ISSN (Print) 1226-1750
ISSN (Online) 2233-6656
Journal of Magnetics 24(3), 429-436 (2019) https://doi.org/10.4283/JMAG.2019.24.3.429

Performance Evaluation of New Nonlocal Total Variation Noise Reduction Algorithm in Parallel Magnetic Resonance Imaging with Sensitivity Encoding Reconstruction

Joo-Wan Hong[1], Kyuseok Kim[2], and Youngjin Lee[3]*

[1]*Department of Radiological Science, Eulji University, 553, Sanseong-daero, Sujeong-gu, Seongnam-si, Gyeonggi-do, Republic of Korea*
[2]*Department of Radiation Convergence Engineering, Yonsei University, 1, Yonseidae-gil, Wonju-si, Gangwon-do, Republic of Korea*
[3]*Department of Radiological Science, Gachon University, 191, Hambakmoe-Ro, Yoensu-Gu, Incheon, Republic of Korea*

(Received 29 May 2019, Received in final form 18 July 2019, Accepted 22 July 2019)

Parallel magnetic resonance imaging (pMRI) can acquire high temporal resolution to obtain anatomical images. Among the parallel-imaging techniques, sensitivity encoding (SENSE) is the most widely used. During the SENSE process, they are previously limited by signal-to-noise ratio degradation and aliasing artifacts owing to the subsampling effect. Therefore, the objective of this study was to develop and evaluate a novel nonlocal total variation (new-NLTV) noise reduction algorithm in pMRI with SENSE reconstruction in both simulation and experiments. According to the results, the proposed algorithm was able to achieve impressive results using quantitative evaluation factors in simulation and real phantom images. The contrast-to-noise ratio and coefficient of variation for the algorithm, in particular, were 8.24 and 7.15 times better, respectively, than those of the noisy image in the phantom study. In conclusion, this study successfully demonstrated the effectiveness of the new-NLTV noise reduction algorithm in pMRI with SENSE reconstruction.

Keywords : parallel magnetic resonance imaging, sensitivity encoding reconstruction, new nonlocal total variation noise reduction algorithm, image processing technique, quantitative evaluation of image performance

1. Introduction

Among frequently used medical-imaging techniques, magnetic resonance imaging (MRI), which creates images with high contrast and spatial resolution for anatomical assessment, is based on the activity of the nuclei in atoms and has an important use in the detection of diseases in the field of medical diagnosis [1, 2].

Formation of a magnetic resonance (MR) image is based on the k-space data in 2D or 3D information by the pulse sequence. The sampling of k-space data by a determined number of phase-encoding steps accounts for the data acquisition time in the acquisition of an MR image [3]. In MRI, basic pulse sequences are used for each purpose: the spin echo and gradient echo in which each gradient is applied in a different direction [4]. However, most pulse sequences have been encoded only once in a gradient, so it is necessary to apply a series of gradients continually to fill a given number of encodings. To overcome this problem, parallel MRI (pMRI), which can acquire a lower scan time (higher temporal resolution) without the loss of spatial resolution, has been developed by several researchers [5].

pMRI has made considerable progress by improving spatial resolution and contrast resolution and decreasing motion artifacts with high temporal resolution [6]. One of the basic methods for scan time reduction without deterioration of image performance is to use a rectangular field of view (FOV) using axial profile information. This method is based on representation of fewer phase encoding steps in the k-space domain. However, an aliasing artifact is caused by a rectangular phase-encoding direction. To cope with this problem, multichannel phased-array coils that were initially developed to enhance the signal-to-noise ratio (SNR) in MR images and restricted rectangular FOV are used [3]. Based on this theory, Pruessmann *et al*. proposed a reconstruction method and strategies with the Fourier transform, *i.e.*, sensitivity encoding (SENSE) [7]. SENSE can acquire an acute coil configuration and sampling pattern with a combination of

*Corresponding author: Tel: +82-32-820-4362
Fax: +82-32-820-4449, e-mail: yj20@gachon.ac.kr

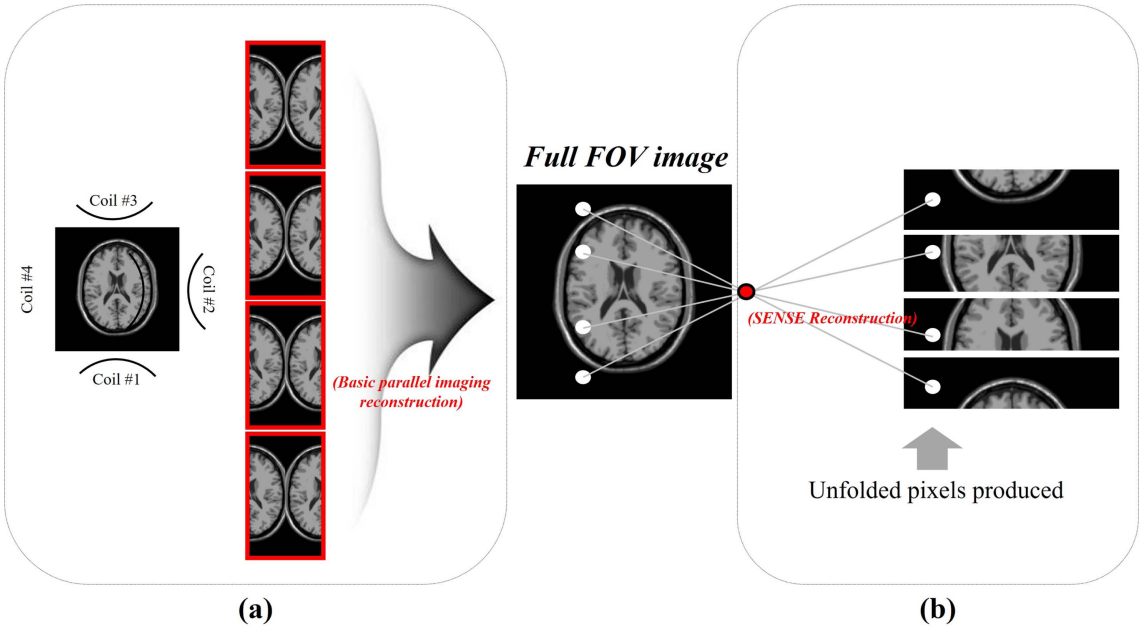

Fig. 1. (Color online) Schematic illustration of reconstruction process for basic parallel imaging and sensitivity encoding (SENSE) with phase array coils.

sensitivity and gradient information. Fig. 1 shows a schematic illustration of basic parallel-imaging reconstruction and SENSE reconstruction.

Noise in pMRI images, including the SENSE reconstruction method, has generally been statistically produced attending to the phased-array coil [8]. In phased-array coil systems, one can acquire an increasing subsampling data acquisition rate in the k-space with the reduction of the phase distortion effect [9]. In addition, in the SENSE reconstruction image, the resulting SNR with full samples is related by the "g-factor." Based on these situations, Fernandez *et al*. estimated a final statistical noise model in SENSE reconstruction with a pMRI system, and the formula is calculated as follows [8].

$$\sigma_i(x, y) = Z_i^* \Sigma Z_i . \quad (1)$$

where $\sigma_i(x, y)$ is the noise variance, and Z_i is position dependent.

All final reconstruction images in pMRI follow an almost complex Gaussian distribution and Rician distribution [10]. To eliminate the noise component effectively, MR denoising with image processing based on software is an important task. Several studies have been conducted to develop a noise reduction algorithm for diagnostic images, including MRI images [11-14]. The processing process of conventional median and Wiener filters is remarkably simple but has a low ratio for noise elimination [15]. To increase the efficiency of noise reduction process, an iterative-based method using a total variation (TV) noise reduction algorithm was developed [16]. In particular, among the iteration-based methods, a novel nonlocal TV (new-NLTV) scheme for denoising has been proposed to overcome the nonuniformity and improve edge preservation in the image [17]. However, there is not much research concerning the application of the new-NLTV noise reduction algorithm in SENSE reconstruction images with pMRI.

The purpose of this study was to develop a new-NLTV noise reduction algorithm and evaluate the image performances in a pMRI image with SENSE reconstruction. For this purpose, simulation and experimental studies were performed using a 3-T MRI system and a homogeneous rectangular phantom. The MRiLab, which is a newly designed, well-validated MRI simulator developed by Liu *et al.*, was used in this study [18]. To evaluate noise characteristics quantitatively, the contrast-to-noise ratio (CNR), coefficient of variance (COV), root mean square error (RMSE), and edge preservation index (EPI) were used in a simulation study, and the CNR, COV, and intensity profile were used in an experimental study.

2. Materials and Methods

2.1. New nonlocal total variation (new-NLTV) noise reduction algorithm modeling

In pMRI systems, noise occurs because of the inherent characteristics of the combination of the original signal and secondary signal (*e.g.*, noise). Liu *et al.* [19]

introduced a new nonlocal total variation (new-NLTV) algorithm for image denoising as follows.

$$\phi(u) = \text{argmin}_u \int_\Omega |D_{NL}u| + \frac{\beta}{2}\|u\|_2^2 + \frac{1}{2}\|u - f\|_2^2, \quad (2)$$

$$D_{NL}u(s, t) = (u(s) - u(t))\sqrt{w(s, t)}, \quad (3)$$

$$w(s, t) = \exp\left\{-\frac{\int_\Omega G_h(x)|f(s+x) - f(t+x)|^2 dx}{2\sigma^2}\right\}, \quad (4)$$

where u is the noise-free image, f is the observed image, $\Omega \subseteq \mathbb{R}^2$ denotes a bounded open subset with a Lipschitzian boundary, β is the balancing parameter, $D_{NL}u$ is the nonlocal gradient of u, $w(s, t)$ is a weighting function, G_σ is the Gaussian kernel of standard deviation, h, and σ is the filtering scale with noise level. For solving the optimization problem in Eq. (2), the split Bregman method [20] operates efficiently as follows.

$$(u^{k+1}, d^{k+1}) = \underset{u, d}{\text{argmin}}\ \alpha|d| + \frac{\beta}{2}\|u\|_2^2 + \frac{1}{2}\|u - f\|_2^2 + \frac{\gamma}{2}\|d - D_{NL}u - b^k\|_2^2, \ s.t.\ d = D_{NL}u, \quad (5)$$

$$u^{k+1} = \text{argmin}_u \frac{\beta}{2}\|u\|_2^2 + \frac{1}{2}\|u - f\|_2^2 + \frac{\gamma}{2}\|D_{NL}u - d^k + b^k\|_2^2 + \frac{P_1}{2}\|u - u^k\|_2^2, \quad (6)$$

$$d^{k+1} = \text{argmin}_d \alpha|d| + \frac{\gamma}{2}\|d - D_{NL}u - b^k\|_2^2 + \frac{P_2}{2}\|u - u^k\|_2^2, \quad (7)$$

$$b^{k+1} = b^k + (D_{NL}u^{k+1} - d^{k+1}), \quad (8)$$

where P_1 and P_2 are positive weights. Computationally, Eq. (6) is derived for solving u^{k+1} as follows.

$$0 = \beta u^{k+1} + (u^{k+1} - f) + \gamma D_{NL}^T(D_{NL}u^{k+1} - d^k + b^k) + P_1(u^{k+1} - u^k), \quad (9)$$

$$u^{k+1} = \frac{f + \gamma div_{NL}(b^k - d^k) + P_1 u^k}{(1 + \beta + P_1 - \gamma(-D_{NL}^T D_{NL}))}, \quad (10)$$

and then, one can obtain the update d^{k+1} using the generalized shrinkage formula [21] as follows:

$$d^{k+1} = \text{sign}\left(\frac{\gamma(D_{NL}u^{k+1} + b^k) + P_2 d^k}{\gamma + P_2}\right) \cdot \max\left(\left|\gamma(D_{NL}u^{k+1} + b^k) + P_2 d^k\right| - \frac{\alpha}{\gamma + P_2}, 0\right). \quad (11)$$

Finally, the appropriate iteration number of the inner loop is applied to obtain a satisfactory denoised result.

2.2. Image acquisition parameter

To study the simulation condition, the new comprehensive MRiLab simulator with a recent graphical processing

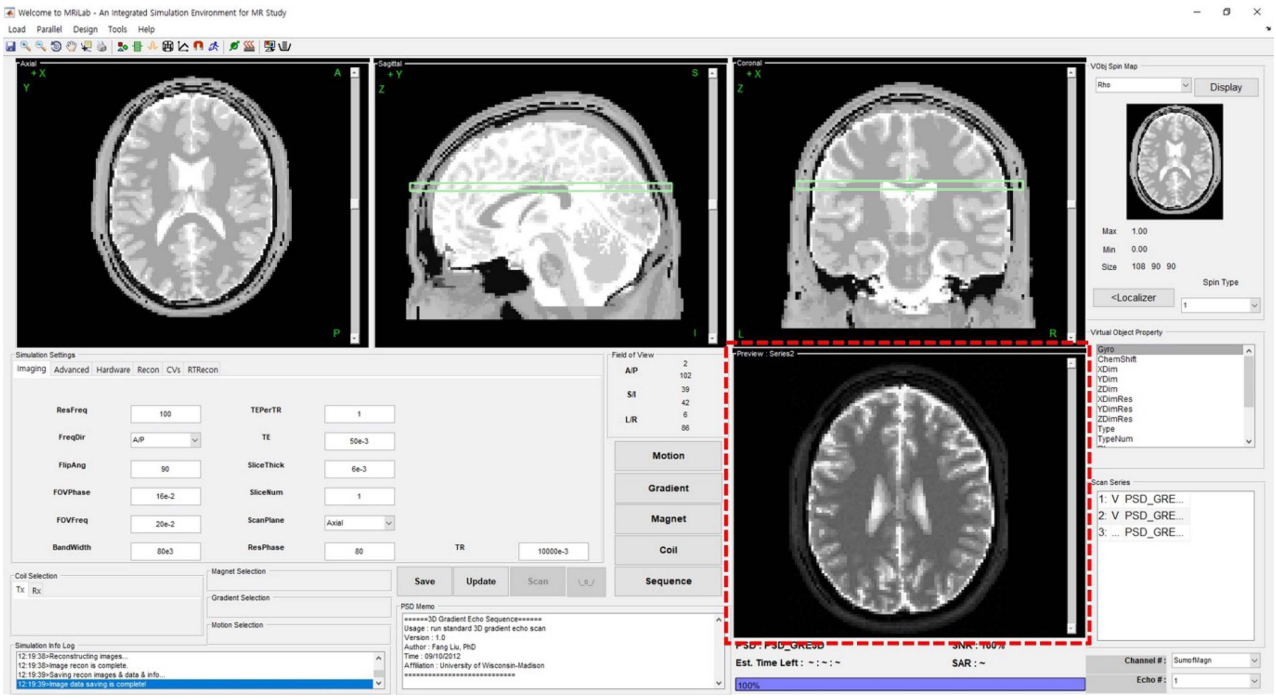

Fig. 2. (Color online) Photo example of MRiLab simulation control console including adjustable MR parameters.

Table 1. MRI data acquisition parameters.

Scan parameter	
Repetition time (TR)	600 msec
Time to echo (TE)	8 msec
Minimum slice gap	5 mm
Maximum slice gap	20 mm
Field of view (FOV)	230 mm
Slice thickness	5 mm
SENSE reconstruction	Yes
Reconstruction voxel size	0.9 mm

unit [18] was used. MRiLab version 1.3 is a newly designed platform that is dedicated to MRI systems. This simulator can model a new phantom design and enhance MR sequence design. The accuracy and efficacy of the MRiLab simulator have been demonstrated by the research group that produced the program. Fig. 2 shows the main simulation control console.

For acquiring a real pMRI image, 3-T MRI devices and an eight-channel phased-array coil were used in this study. Table 1 shows the MR acquisition parameters.

2.3. Image quality analysis

The image characteristics in terms of the profile, CNR, COV, RMSE, and EPI were investigated quantitatively. The CNR formula can be written as follows.

$$CNR = \frac{\left|\bar{\mu}_{ROI_1} - \bar{\mu}_{ROI_2}\right|}{\sqrt{\bar{\sigma}^2_{ROI_1} - \bar{\sigma}^2_{ROI_2}}}, \tag{12}$$

where $\bar{\mu}$ and $\bar{\sigma}$ are the mean and standard deviation in the region of interest (ROI) (a rectangular ROI in this case; for example, ROI_1 and ROI_2 in Figs. 3 and 6), respectively. Here, the CNR value is presented as a factor for quantitatively determining the contrast considering noise fluctuations in the ROI. The COV value can be defined as follows:

$$COV = \frac{\sigma}{\mu}. \tag{13}$$

The small COV value indicates the lower noise fluctuation in the ROI. The RMSE is expressed as the difference between the data of the exact image ($\mu_{x,y}$) and the estimated image ($\hat{\mu}_{x,y}$).

$$RMSE(x, y) = \sqrt{\frac{\Sigma_{i=1}^{N}(\mu_{x,y} - \hat{\mu}_{x,y})^2}{\Sigma_{i=1}^{N}(\hat{\mu}_{x,y})^2}}, \tag{14}$$

where x and y are the indices of the data in the image domain. Here, the smaller the RMSE, the greater the resemblance to the "gold standard" image. The EPI factors can be expressed mathematically as follows.

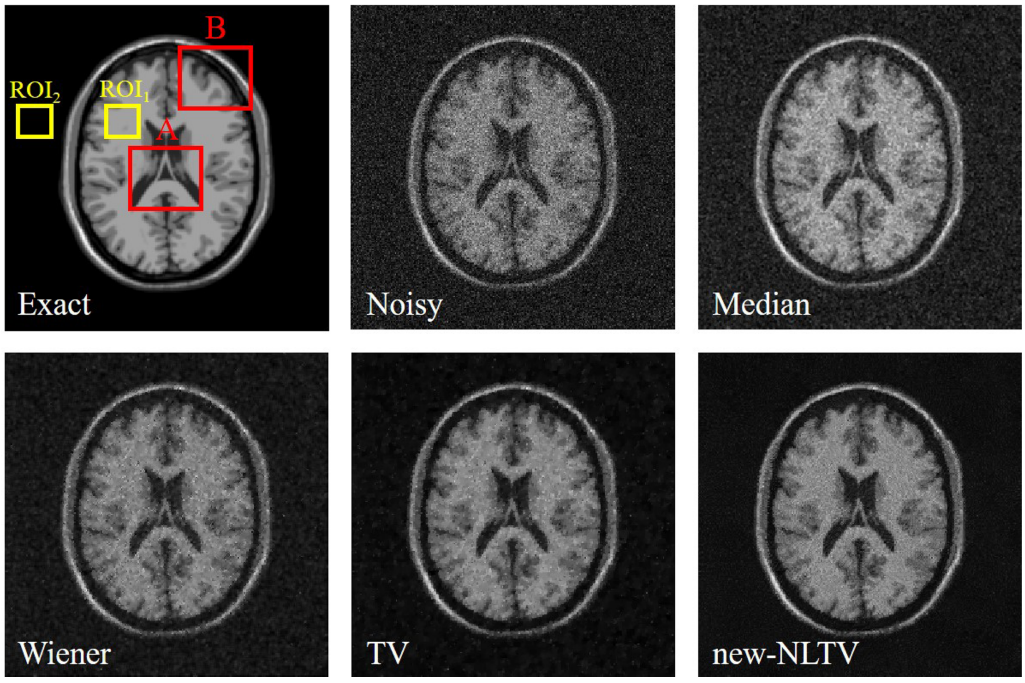

Fig. 3. (Color online) Simulation results of exact image (top left), noisy image (top middle), denoised image with median filter (top right), denoised image with Wiener filter (bottom left), denoised image with total variation (TV) (bottom middle), and denoised image with new-nonlocal TV (new-NLTV) (bottom right).

$$EPI = \frac{\Gamma(\Delta q_1 - \overline{\Delta q_1}, \Delta q_2 - \overline{\Delta q_2})}{\Gamma(\Delta q_1 - \overline{\Delta q_1}, \Delta q_1 - \overline{\Delta q_1}) \circ \Gamma(\Delta q_2 - \overline{\Delta q_2}, \Delta q_2 - \overline{\Delta q_2})}, \quad (15)$$

$$\Gamma(x, y) = \Sigma_{x,y \in ROI} a(x, y) \circ b(x, y), \quad (16)$$

where $\overline{\Delta q}$ is the mean of the Laplacian filtered images of the ROI (in this study, 3 × 3 pixels were used) using the exact image (q_1) and the estimated image (q_2). The EPI value has a range of 0 to 1, and the closer this value is to 1, the sharper the edge structure in the image. The details of the EPI have been investigated extensively in the literature [22].

3. Results and Discussion

In the medical diagnosis field, pMRI with SENSE reconstruction is growing exponentially in use, because the device can provide excellent anatomical information.

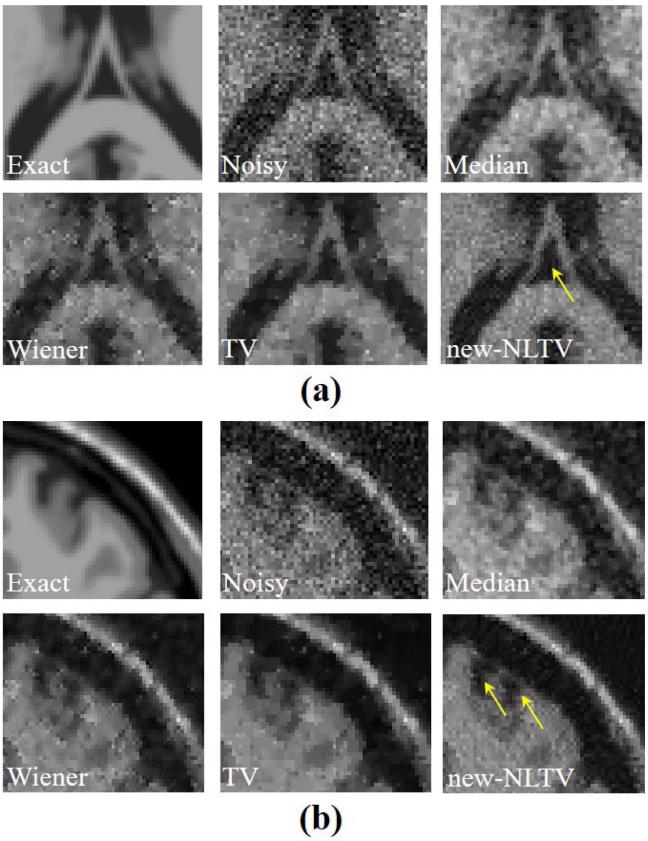

Fig. 4. (Color online) The enlarged images of exact image (top left), noisy image (top middle), denoised image with median filter (top right), denoised image with Wiener filter (bottom left), denoised image with TV (bottom middle), denoised image with new-NLTV (bottom right), indicated in (a) box *A* and (b) box *B* of Fig. 3.

In pMRI images, noise reduction by using an image-processing method is particularly important. The purpose of this study was to use a newly develop denoising algorithm based on a nonlocal approach and to apply the acquired pMRI image with SENSE reconstruction.

In this study, a brain MR image was acquired, and noise was added in the image by using the MRiLab simulator. Fig. 3 shows the simulation results of the exact image (top left), the noisy image (top middle), denoised image with median filter (top right), denoised image with Wiener filter (bottom left), denoised image with TV (bottom middle), and denoised image with new-NLTV (bottom right). Fig. 4 shows the enlarged images of the exact image (top left), noisy image (top middle), denoised image with median filter (top right), denoised image with Wiener filter (bottom left), denoised image with TV (bottom middle), and denoised image with new-NLTV (bottom right), as indicated in boxes *A* and *B* of Fig. 3. The denoised image using new-NLTV shows better image characteristics than the noisy and the other denoised images while preserving the edge components.

For the quantitative evaluation using a simulated brain MR image, the CNR, COV, RMSE, and EPI characteristics were measured, and the results are listed in Fig. 5. Figs. 5 (a) and (b) show that the CNR values are approximately 4.58 (noisy image), 6.02 (denoised image with median filter), 7.70 (denoised image with Wiener filter), 9.17 (denoised image with TV), and 17.95 (denoised image with new-NLTV), and the COV values are 6.75 (noisy image), 5.12 (denoised image with median filter), 2.17 (denoised image with Wiener filter), 1.11 (denoised image with TV), and 0.75 (denoised image with new-NLTV). By comparing the denoising methods, the CNR results for the proposed new-NLTV denoising technique were approximately 3.92, 2.98, 2.33, and 1.96 times higher than those of the noisy image, median filter, Wiener filter, and TV denoising algorithm, respectively. In addition, the COV results for the proposed new-NLTV denoising technique were approximately 9.00, 6.83, 2.89, and 1.48 times better than those of the noisy image, median filter, Wiener filter, and TV denoising algorithm, respectively.

Fig. 5(c) shows that the RMSE values of the denoised image with new-NLTV are approximately four times smaller than those of the noisy image: 8.41 (noisy image), 6.34 (denoised image with median filter), 4.13 (denoised image with Wiener filter), 3.68 (denoised image with TV), and 2.72 (denoised image with new-NLTV). The simulated RMSE increased in order for the proposed new-NLTV denoising technique, TV denoising algorithm, Wiener filter, median filter, and noisy image. When compared with the denoising methods, the RMSE results

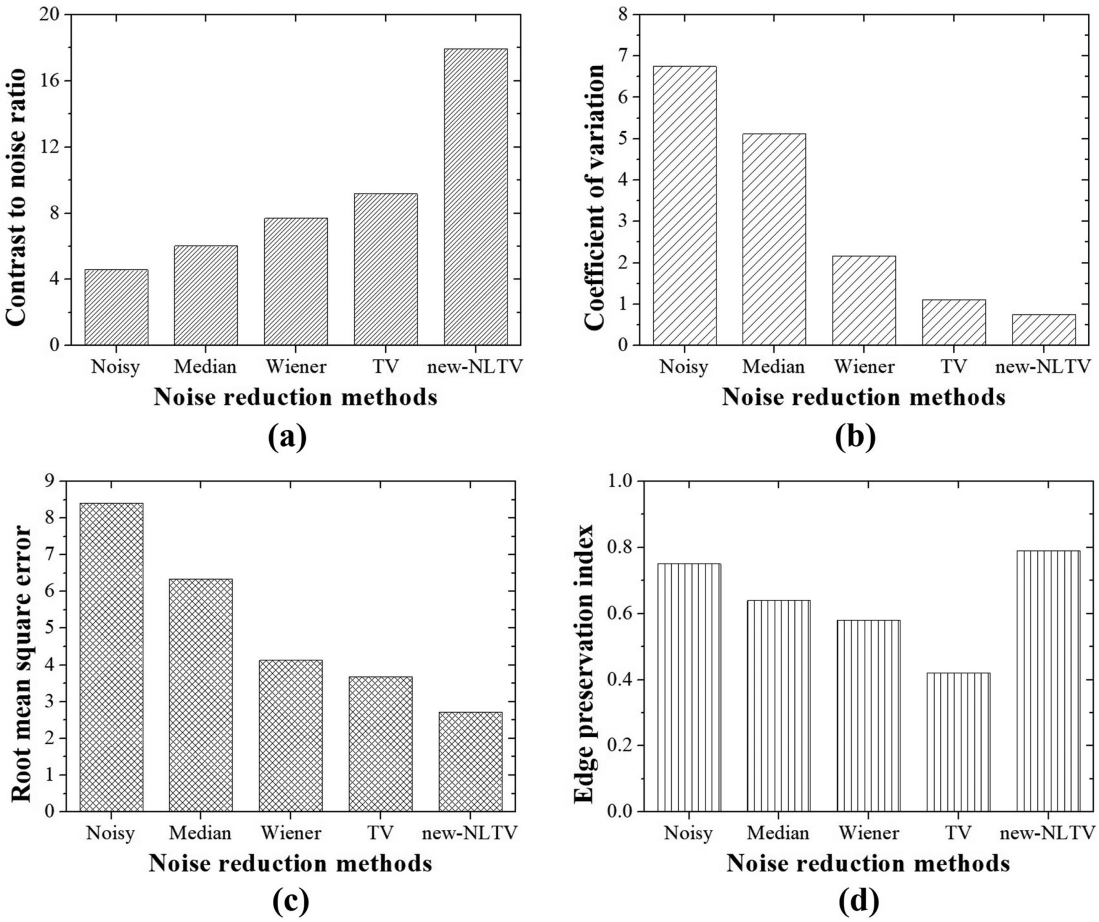

Fig. 5. (Color online) Evaluated (a) CNR and (b) COV indicated by predefining regions of interest (ROIs) (*i.e.*, ROI_1 and ROI_2 in Fig. 3) and measured (c) RMSE and (d) EPI by means of the exact image for reference in simulation condition.

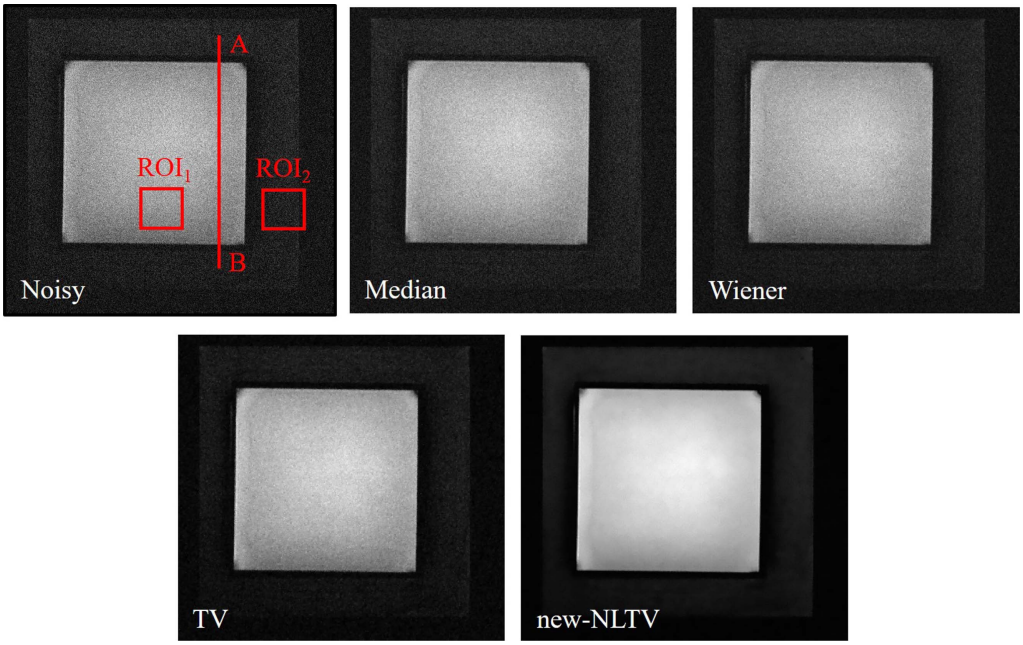

Fig. 6. (Color online) Experiment results of noisy image (top left), denoised image using median filter (top middle), denoised image using Wiener filter (top right), denoised image using TV (bottom left), and denoised image using new-NLTV (bottom right).

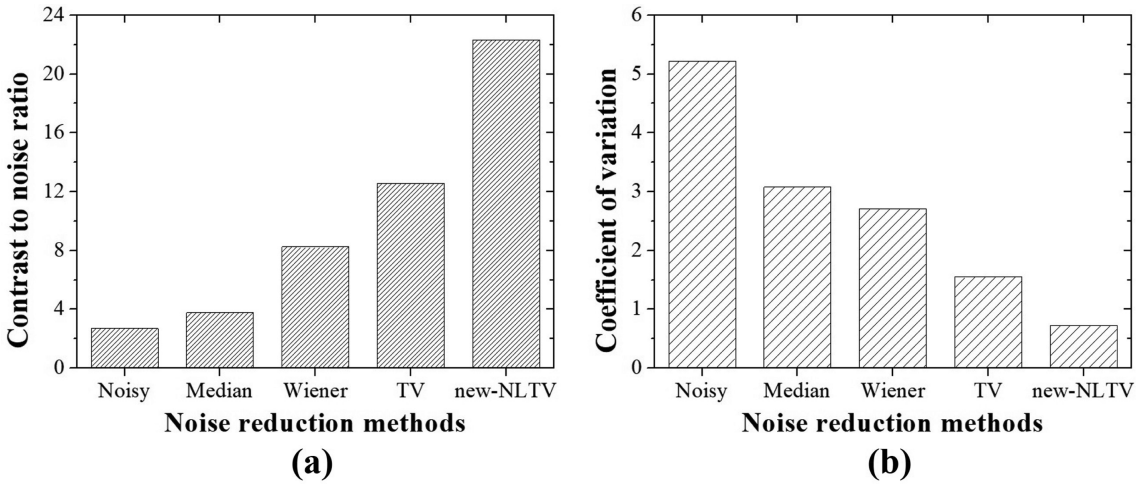

Fig. 7. Measured (a) CNR and (b) COV indicated by predefining regions of interest (ROIs) (*i.e.*, ROI_1 and ROI_2 in Fig. 6).

using the proposed new-NLTV denoising technique were approximately 3.09, 2.33, 1.52, and 1.35 times better than those of the noisy image, median filter, Wiener filter, and TV denoising algorithm, respectively.

The EPI value of the denoised image with new-NLTV is closer to that of the noisy image rather than those of denoised images — see Fig. 5(d). The evaluated EPI increased in order for the TV denoising algorithm, Wiener filter, median filter, noisy image, and the proposed new-NLTV denoising technique. The results indicate that the new-NLTV algorithm can rarely be effectively operated to reduce the noise without edge smoothing in pMRI.

Fig. 6 shows the experiment results for the noisy image (top left), denoised image using median filter (top middle), denoised image using Wiener filter (top right), denoised image using TV (bottom left), and denoised image using new-NLTV (bottom right).

Fig. 7 shows the bar graphs of the measured CNR and COV indicated in boxes ROI_1 and ROI_2 of Fig. 6. The CNR results are approximately 2.71 (noisy image), 3.78 (denoised image with median filter), 8.24 (denoised image with Wiener filter), 12.57 (denoised image with TV), and 22.34 (denoised image with new-NLTV), and the COV values are 5.22 (noisy image), 3.08 (denoised image with median filter), 2.71 (denoised image with Wiener filter), 1.55 (denoised image with TV), and 0.73 (denoised image with new-NLTV). A comparison of the denoising methods shows that the CNR results for our proposed new-NLTV denoising technique were approximately 8.24, 5.91, 2.71, and 1.78 times higher than those of the noisy image, median filter, Wiener filter, and TV denoising algorithm, respectively. In addition, the COV results for the proposed new-NLTV denoising technique were approximately 7.15, 4.22, 3.71, and 2.12 times better than those of the noisy image, median filter, Wiener filter, and TV denoising algorithm, respectively.

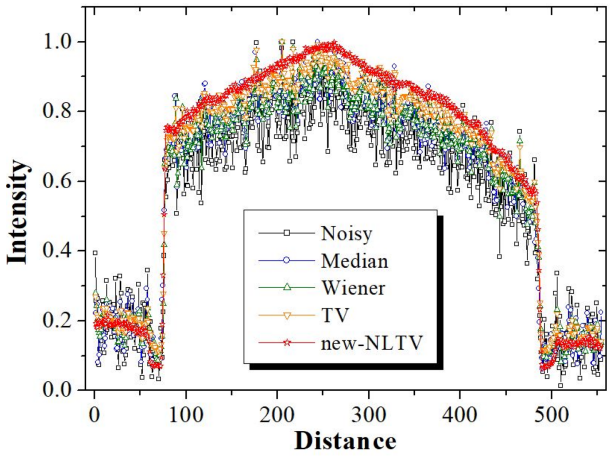

Fig. 8. (Color online) Measured 1D profiles indicated by red line $\overline{AB}$ in Fig. 6.

Fig. 8 shows the intensity profiles measured along the $\overline{AB}$ line segments indicated in Fig. 6. Compared with the profiles of the other images, the profile of the denoised image using the new-NLTV algorithm shows that it is highly effective in reducing the noise component. In addition, we confirmed that NLTV algorithm can provide various findings of fundamental in MRI image including image stabilization.

4. Conclusion

Although the pMRI technique is a practical method with several useful applications, a noise reduction process is essential in the image. According to the results, the quantitative evaluation parameters for the proposed new-

NLTV algorithm were better than those of the noisy image and previously used algorithm or filter both in simulation and experimental studies. In conclusion, the results indicate that the proposed algorithm is effective for denoising in pMRI with SENSE reconstruction.

Acknowledgment

The research was supported by the National Research Foundation of Korea (NRF-2016R1D1A1B03930357). Also, Joo-Wan Hong and Kyuseok Kim contributed equally to the writing of this paper.

References

[1] P. C. Lauterbur, Nature **242**, 190 (1973).
[2] X. Yan, J. C. Gore, and W. A. Grissom, Nature Communications **9**, 1 (2018).
[3] J. F. Glockner, H. H. Hu, D. W. Stanley, L. Angelos, and K. King, RadioGraphics **25**, 1279 (2005).
[4] R. Bitar, G. Leung, R. Perng, S. Tadros, A. R. Moody, J. Sarrazin, C. McGregor, M. Christakis, S. Symons, A. Nelson, and T. P. Roberts, RadioGraphics **26**, 513 (2006).
[5] J. Hamilton, D. Franson, and N. Seiberlich, Prog. Nucl. Magn. Reson. Spectrosc. **101**, 71 (2017).
[6] P. Noel, R. Bammer, C. Reinhold, and M. A. Haider, Can. Assoc. Radiol. J. **60**, 91 (2009).
[7] K. P. Pruessmann, M. Weiger, M. B. Scheidegger, and P. Boesiger, Magn. Reson. Med. **42**, 952 (1999).
[8] S. A. Fernandez, G. V. S. Ferrero, and A. T. Vega, Magn. Reson. Imaging **32**, 281 (2014).
[9] W. S. Hoge, D. H. Brooks, B. Madore, and W. E. Kyriakos, Concepts in Magnetic Resonance Part A **27**, 17 (2005).
[10] P. Thunberg and P. Zetterberg, Magn. Reson. Imaging **25**, 1089 (2007).
[11] H. V. Bhujle and B. H. Vadavadagi, Biomed. Sign. Process. Control **47**, 252 (2019).
[12] V. N. P. Raj and T. Venkateswarlu, IJMA **4**, 53 (2012).
[13] D. Ai, J. Yang, J. Fan, W. Cong, and X. Wang, Optik **126**, 3844 (2015).
[14] O. Dietrich, J. G. Raya, S. B. Reeder, M. F. Reiser, and S. O. Schoenberg, J. Magn. Reson. Imaging **26**, 375 (2007).
[15] S. Lee, H. Cho, and Y. Lee, Nucl. Instrum. Meth. Phys. Res. A **925**, 212 (2019).
[16] K. Seo, S. H. Kim, S. H. Kang, J. Park, C. L. Lee, and Y. Lee, J. Magn. **21**, 593 (2016).
[17] H. Kim, J. Chen, A. Wang, C. Chuang, M. Held, and J. Pouliot, Phys. Med. Biol. **61**, 6878 (2016).
[18] F. Liu, J. V. Velikina, W. F. Block, R. Kijowski, and A. A. Samsonov, IEEE Trans. Med. Imaging **36**, 527 (2017).
[19] X. Liu and L. Huang, AJR **187**, Math. Comput. Simul. **97**, 224 (2014).
[20] T. Goldstein and S. Osher, SIAM J. Imaging Sci. **2**, 323 (2009).
[21] W. Yin, S. Osher, D. Goldfarb, and J. Darbon, SIAM J. Imaging Sci. **1**, 143 (2008).
[22] F. Satter, L. Floreby, G. Salomonsson, and B. Lovstrom, IEEE Trans. Image Process. **6**, 888 (1997).